

Disturbance Field Decomposition in a Transversely Forced Swirl Flow and Flame

Jacqueline O'Connor
Pennsylvania State University, University Park, Pennsylvania

1 Abstract

High amplitude combustion instabilities are a destructive and pervasive problem in gas turbine combustors. Although much research has focused on measuring the characteristics of these instabilities, there are still many remaining questions about the fluid-mechanic mechanisms that drive the flame oscillations. In particular, a variety of complex disturbance mechanisms arise during velocity-coupled instabilities excited by transverse acoustic modes. The resulting disturbance field has two components – the acoustic velocity fluctuation from both the incident transverse acoustic field and the excited longitudinal field near the nozzle, and the vortical velocity fluctuations arising from acoustic excitation of hydrodynamic instabilities in the flow. In this research, we look at the relative contribution of these two components using proper orthogonal decomposition as a methodology for decomposing the velocity disturbance field. While POD is successful at decomposing these two components at certain non-reacting conditions, it fails at reacting conditions. These results show the significant interaction of velocity disturbance modes under reacting conditions and the limitations of the POD technique for extracting velocity decomposition information.

2 Nomenclature

Abbreviations	Meaning
A	Amplitude
D	Outer diameter of nozzle
PIV	Particle image velocimetry
POD	Proper orthogonal decomposition
Re_D	Reynolds number based on nozzle diameter, D
SVD	Singular value decomposition
U_o	Bulk velocity
r	Radial coordinate
r_1	Inner radius of annular jet
r_2	Outer radius of annular jet
t	Time
\vec{u}	Velocity vector
x	Axial coordinate

α	Vorticity decay rate
ϕ	Phase difference
ω	Angular frequency

Scripts	Meaning
L	Longitudinal
T	Transverse
c	Convective
<i>acoustic</i>	Acoustic component
o	Bulk
<i>vortical</i>	Vortical component

3 Introduction

Combustion instability in annular gas turbine engines is a pressing issue for both aircraft engines and power generation gas turbines. Driven by the coupling between flame heat release rate fluctuations and acoustically-excited disturbances in the combustor [1], combustion instability can lead to reduced operability, increased emissions, and hardware damage [2]. While mitigation strategies for reducing the impact of combustion instability are available [3, 4], better understanding of these instabilities can help develop predictive tools for avoiding instability regimes during operation [5, 6].

This study focuses on understanding phenomena present during transverse instabilities in annular combustor systems, particularly those driven by circumferential acoustic modes. These modes, in the 100's of Hertz range [7], raise additional complexity as compared to longitudinal acoustic modes, which have been the focus of study for some time [8-14]. First, circumferential modes can be either standing-wave modes or spinning modes, and the prediction of the mode is sensitive to the boundary conditions that enforce the mode shape [15]. In either of these cases, the flame response may vary from nozzle to nozzle, as each flame is located at a different portion of the acoustic mode during an acoustic cycle. This makes prediction of combustion instability in a full-annular configuration complex as the response of each nozzle may need to be considered individually.

Next, disturbances near the flame, both pressure and velocity disturbances, can be non-axisymmetric with respect to the streamwise flame axis [16], as opposed to the symmetric disturbances present during longitudinal instabilities. This non-axisymmetry adds a layer of complexity to understanding both the disturbance field itself [17] as well as the response of the flow field and flame [18]. Recent experimental [19] and theoretical [20] work has shown that the net heat release rate fluctuation across an acoustic cycle

of a time-average symmetric flame is only a function of the symmetric portion of the velocity disturbance field. This means that purely non-axisymmetric disturbances, within the linear regime, do not contribute to the thermoacoustic feedback cycle for axisymmetric flames. However, flames typically are not axisymmetric in real combustion systems, particular high-aspect-ratio geometries like annular combustors, and so the response to non-axisymmetric transverse excitation is a complex function of both the non-axisymmetry of the time-averaged flame shape and the velocity disturbance field. The role of both flame and disturbance field symmetry is currently the focus of on-going work.

Finally, transverse, non-axisymmetric forcing introduces additional possible velocity-coupling mechanisms between the disturbance field and the flame as compared to the longitudinal mode. Previous work by this author [21, 22] and others [23, 24] have identified several possible velocity disturbance pathways from the incident transverse acoustic field to the flame heat release rate fluctuations that drive the instability. In general, the relevant velocity disturbances in these combustion systems can be categorized into two types: acoustic disturbances and vortical disturbances [22, 25]. Acoustic velocity disturbances propagate at the speed of sound and influence the flame heat release rate fluctuations both at the base of the flame – via a base-wave mechanism [26] – and locally along the flame front. In the transversely forced system, there are two sources of acoustic velocity disturbances: the incident transverse acoustic field and the longitudinal acoustic field that is excited by pressure fluctuations from the transverse acoustic field above the nozzle exit. This coupling mechanism has been described by several authors in the transverse instability literature [17, 21, 27, 28] and is the focus of much research in the rocket community, where it is termed “injector coupling” [29]. In the current configuration, the flame is acoustically compact, meaning that the transverse acoustic wavelength is much longer than any dimension of the flame. When the flame is located at a pressure node, or velocity anti-node, the net acoustic velocity fluctuation through the flame is roughly zero, leading to little net flame response from the acoustic disturbance pathway. However, when the flame is located at a pressure anti-node, or velocity node, the transverse to longitudinal acoustic coupling can drive significant flame response to acoustic fluctuations [28, 30].

Vortical velocity fluctuations are excited by the acoustic fluctuations and convect at a velocity on the order of the mean flow. They can take many forms, including shear layer excitation [31], vortex breakdown bubble excitation [11, 14], and swirl fluctuation [9, 10]. These vortical disturbances excite wrinkles along the flame front and can lead to significant heat release rate fluctuations. In the current configuration, the dominant vorticity fluctuation mechanism is through shear layer rollup along the flame. Previous work on this particular flow field has shown that the vortex breakdown bubble dynamics are limited as a result of the merging of the vortex breakdown bubble with the centerbody recirculation zone, and the stagnation boundary condition on the face of the centerbody [18]. At the acoustic velocity node, pressure anti-node

forcing condition, the shear layer response is predominantly symmetric and vortex rings are shed in both the inner and outer shear layers; flame response stems from the vortex shedding in the inner shear layer as the flame is stabilized there. The non-axisymmetric forcing condition, with a pressure node and velocity anti-node, results in helical vortex shedding in the inner and outer shear layers and non-axisymmetric flame response.

Finally, traditional disturbance decomposition methods also identify an entropy disturbance component that can arise in combustion systems. Following Chu and Kovasznay [25], a disturbance field can be decomposed into a vortical, acoustic, and entropy disturbance; the entropy component of the velocity disturbance field is non-rotational, and the divergence of this component of the field is equal to the time rate of change of the fluid entropy normalized by the constant-pressure specific heat. A scaling analysis of these disturbances shows that the entropy component of the velocity disturbance field is very small compared to that of the acoustic and vortical components, and so it is neglected in this analysis.

The relative contribution of acoustic and vortical velocity fluctuations to overall flame response is difficult to measure. This is in large part because it is challenging to decompose the velocity disturbance field into the acoustic and vortical components in experimental data. A number of researchers have used Curle's analogy to obtain the acoustic pressure field from PIV data, which can then be used to calculate the acoustic velocity component and separate it from the vortical velocity component [32-34]. However, this analogy is typically applied to self-excited systems where the boundary conditions of the measurement volume are very well defined. In the present research, this decomposition would be intractable because the boundary conditions are not well defined as a result of the external acoustic excitation. Additionally, the disparate length scales between the acoustic (on the order of meters) and vortical (on the order of millimeters) fluctuation length scales makes separation of these disturbances difficult. Further, background noise in the data may contaminate the acoustic velocity component calculation to the point of being unphysical.

Previous work by the author has used a two-equation model to attempt to capture the key components of the acoustic and vortical velocity disturbances [35], as is shown in Equation 1. In this model, the acoustic and vortical disturbances are assumed to be harmonic and at the same frequency, which is equal to the forcing frequency. The phase speed of the acoustic disturbance is assumed to be infinite, meaning that the acoustic wave is a standing wave. The phase speed, $u_{c,v}$, and decay rate, α , of the vortical wave is calculated from the Fast Fourier Transform (FFT) of the vorticity fluctuations along the shear layers, and the convection speed of the vortical disturbances is within the previously reported bounds of 0.5 to 1.5 times the mean flow speed [36].

$$\begin{aligned}
u_{acoustic} &= A_1 e^{-i(\omega t + \phi)} \\
u_{vortical} &= A_2 e^{-i\omega(t - x/u_{c,v})} e^{-\alpha x}
\end{aligned}$$

Equation 1

Unfortunately, the two-equation model required the use of a curve-fit to determine the amplitude of each wave and the phase between the waves. The vortical disturbance amplitude and phase have been shown in analytical work to be two controlling parameters of the resultant flame heat release rate oscillations [26]. The goal of this study is to extend the previous work using the two-equation model to determine not only the amplitude and phase between the vortical and acoustic velocity disturbances, but also the characteristics of each of these disturbance components with transverse acoustic forcing. The proper orthogonal decomposition (POD) is used in an attempt to separate the acoustic velocity fluctuations and the vortical velocity fluctuations [37]. Although these fluctuation modes will not be automatically separated by the POD, investigation across a range of acoustic forcing conditions has shown that for non-reacting flows, the transverse acoustic fluctuation mode can sometimes be separated into its own eigenmode and that as the amplitude of forcing increases, this eigenmode increases in energy. The results in this work show that this methodology does not work as well for reacting flows, likely as a result of “acoustic shielding” and reflections of the acoustic field by the flame [38]. Despite this, we can learn about the relative contribution of the acoustic and vortical velocity disturbances in the flow field from this decomposition. Understanding the relative contribution of these disturbances can help support model validation and further our understanding of disturbance mechanisms during thermoacoustic instability.

The remainder of this paper is organized as follows. First, an overview of the experimental facility provides details about the combustor, the acoustic forcing configuration, the diagnostics, and the test matrix. Next, the data analysis methods are briefly explained. Results for both the time-averaged and time-varying components of the flow field are provided for both non-reacting and reacting flow. Here, we use the POD to decompose the flow field into its vortical and acoustic components for certain data sets. Finally, we draw conclusions about this work and its application towards better understanding and controlling combustion instabilities in gas turbines.

4 Experimental overview

A single-nozzle combustor with transverse-forcing capability is used in this series of tests, as shown in Figure 1 and discussed in great detail in Ref. [39]. This high-aspect-ratio combustor configuration is used to mimic both the dimensions and acoustic mode of an annular combustion chamber. The inner dimensions of the combustion chamber are 114.3 cm x 35.56 cm x 7.62 cm, with the long dimension in the transverse direction. The nozzle is located at the center of the long dimension and the five 5.08 cm exhaust ports are

located 35.56 cm downstream. The center exhaust port, located directly downstream of the nozzle, is covered with optical-grade quartz glass in these tests to protect the laser optics downstream. The nozzle has an outer diameter of 3.18 cm and a centerbody with a diameter of 2.18 cm. The 12-bladed, non-aerodynamic swirler is located 5.08 cm upstream of the dump plane and has a geometric swirl number of 0.85 [40]. Upstream of the swirler is a large settling chamber that is used to both reduce incoming turbulence and acoustically isolate the combustor from the air and fuel lines. A perforated plate is located inside the chamber to break up large-scale turbulent structures from the air/fuel feed line.

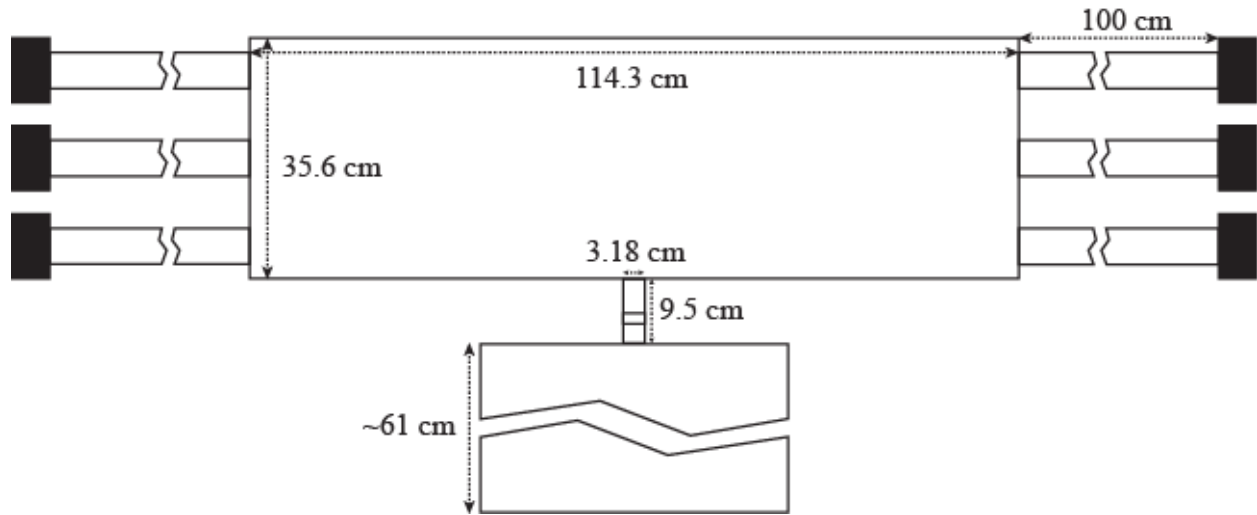


Figure 1. Experimental setup with combustor dimensions, acoustic drivers, and settling chamber. Diagnostics not shown.

In both non-reacting and reacting experiments, air is supplied with a bulk velocity of 10 m/s at the nozzle exit. The turbulence intensity at the inlet is 5.8 m/s, calculated using the axial and radial velocity components. In the reacting experiments, natural gas is mixed with the air well upstream of the settling chamber and can be assumed to be fully premixed; the equivalence ratio is 0.9. The exhaust is far downstream of the exit ports of the combustor, as can be seen in Figure 1.

4.1 Acoustic forcing

Acoustic forcing is used in this experiment to mimic the behavior of self-excited instabilities in annular combustion systems where transverse modes are most likely to occur. Numerous studies have shown that open-loop forcing of combustion systems faithfully mimics the behavior of self-excited systems and excites the same coupling mechanisms that drive combustion instability in realistic combustor geometries. In particular, previous work from this author and others [41, 42] has shown that coupling mechanisms and flame response to transverse acoustics in this experimental facility captures the key dynamics of flames in an annular combustor geometry.

To create this transverse acoustic wave, acoustic forcing is provided by two sets of three speakers, one set on either end of the combustor. The speakers are located at the end of extendable tubes, tuned to 100 cm in these experiments. The speaker tubes attach to the combustor at the end of the long dimension to avoid acoustic streaming in the region of the nozzle. These two banks of speakers are operated so as to create a standing-wave pattern in the combustor; both preliminary experimental work and extensive acoustic modeling using Comsol Multiphysics [17] have indicated that the transverse acoustic mode is planar in the region of the nozzle over a frequency range of approximately 400-1200 Hz. This planar mode is facilitated by hard-wall boundary conditions throughout the combustor (the refractory brick that lines the combustor), with the exception of the nozzle, the coupling between the acoustic forcing tubes and the combustor, and the exhaust outlets. The exhaust outlets are four 5 cm holes at the exit of the combustor, as discussed in Ref. [39].

Two modes of the standing wave are investigated. First, when the two banks of speakers are operated in-phase, this creates a pressure anti-node at the nozzle and will be referred to as “in-phase forcing.” Next, when the two banks of speakers are operated at a phase of 180°, a pressure node is created at the nozzle; this will be referred to as “out-of-phase forcing.” Spatial averages of the transverse flow velocities are calculated in order to determine representative values of the amplitude of acoustic forcing at each condition. The reference transverse velocity fluctuation is obtained from an average of local values over one outer jet diameter downstream along the centerline of the flow. The Fourier transform of the integrated velocity is then calculated and the amplitude at the forcing frequency extracted. Achievable amplitudes at a variety of forcing conditions in this facility have been reported by O’Connor and Lieuwen [43].

In the present study, we only consider the out-of-phase forcing conditions in order to test the applicability of POD to capturing acoustic versus vortical motion. At the in-phase forcing condition, the transverse acoustic velocity fluctuations are relatively small in the field of view and so the decomposition likely won’t be applicable. Instead, we focus on a condition where vortical and acoustic velocity fluctuations are of comparable strengths, and for this experimental condition that necessitates out-of-phase forcing. Several tests are performed to understand the effect of amplitude on the velocity disturbance field in the transversely forced swirling flow. Table 1 provides a list of data that are discussed in this study.

Table 1. Test matrix for velocity measurements.

Frequency [Hz]	Forcing	Amplitude range [m/s]	Reacting/Non
400	Out-of-phase	1, 2, 4.2, 6	non-reacting
400	Out-of-phase	4.2, 6	reacting

4.2 Diagnostics

Velocity measurements in this study are made using high-speed particle image velocimetry (PIV). The laser is a Litron Lasers Ltd. LDY303He Nd:YLF laser with a wavelength of 527 nm and a 5 mJ/pulse pulse energy at the 10 kHz repetition rate used for these experiments. The Photron HighSpeed Star 1.1 camera has a 640x448 pixel resolution with 20x20 micron pixels on the sensor at a frame rate of 10 kHz. A LaVision divergent sheet optic, with an $f = -20$ mm cylindrical lens, is used to create a 1 mm thick sheet. The sheet enters the experiment from a window at the exit plane of the combustor and reaches a width of approximately 12 cm at the dump plane. Aluminum oxide seed particles with a mean diameter of 2 microns are used as flow tracers. Image pairs are taken with a separation time, dt , of nominally 20 microseconds.

Velocity field calculations are performed using DaVis 7.2 software from LaVision. The velocity calculation uses a three-pass operation: the first pass at an interrogation window size of 64x64 pixels, the second two passes at an interrogation window size of 32x32, each with an overlap of 50%. The spatial resolution of the final calculation is 2.3 mm per interrogation window. Each successive calculation uses the previously calculated velocity field to better refine the velocity vector calculation; standard image shifting techniques are employed in the calculation. The correlation peak is found with two, three-point Gaussian fits, and average values of the correlation peak ranged from 0.4 to 1 throughout the velocity field. There are three vector rejection criteria used both in the multi-pass processing steps and the final post-processing step. First, velocity vectors with magnitudes greater than 25 m/s are rejected as unphysical for this specific flow. Second, median filtering is used to filter points where surrounding velocity vectors have an RMS value greater than three times the local point. This filter is used to rid the field of spurious vectors that occur due to issues with imaging, particularly near boundaries. Third, groups of vectors greater than five vectors were removed; this operation removes errors caused by local issues with the original image, including window spotting, and are aggravated by using overlapping interrogation windows. Finally, vector interpolation is used to fill the small spaces of rejected vectors. Overall, an average of 8% of vectors are rejected and replaced with interpolated values.

4.3 Data Analysis

The main data analysis method used in this study is a POD of the velocity field into spatial and temporal eigenmodes [37]. This is a common decomposition method for flow fields that helps to illustrate the major contributions to the fluctuating disturbance field. The results of this analysis produce a spatial mode shape and a temporal mode amplitude; here the FFT of the temporal mode amplitude is presented in order to analyze the spectral content of each mode's oscillation.

In this analysis, 500 instantaneous, two-dimensional velocity fields from PIV are used to calculate the modes, where the data are obtained at 10 kHz. The time-average field is subtracted from the data before the POD analysis so as to only decompose the fluctuating component. An singular value decomposition (SVD) method is used for calculating the POD. At each instant in time, the axial and radial component velocities are converted into a 2240x1 vector, and the SVD decomposition is applied to the 2240x500 matrix of all the data. The 2240x2240 “U” matrix contains the spatial modes, and the 500x500 “V” matrix contains the temporal modes. The units on these modes are arbitrary and should only be interpreted relative to other modes, not to the original flow field. The 2240x500 “ Σ ” matrix contains the energy in each mode, or the singular values of the decomposition. These energies have been non-dimensionalized and reported in percent form. Finally, the flow field can be reconstructed from any number of modes by a matrix multiplication of “U,” “ Σ ,” and transpose “V” matrices.

5 Results

5.1 Time-average flow field

The time-averaged flow field is typical of a highly swirling flow field; an annular jet surrounds a large vortex breakdown region along the centerline. The time-averaged flow field is provided in Figure 2 for both non-reacting (left) and reacting (right) flows. In the axial velocity field, the annular jet is shown originating from the annular gap, and it passes around the centrally located wake/vortex breakdown region. The shear layers shown in the time-averaged vorticity plot arise from the mixing of the annular jet and the inner recirculation zone, forming the inner shear layer, and the quiescent flow around the jet, forming the outer shear layer. The inner shear layer is stronger than the outer, presumably because the velocity gradient between the jet and the recirculating flow in the vortex breakdown region is greater than that between the jet and the quiescent fluid outside the jet.

The time-averaged flow fields of the non-reacting and reacting cases differ in several ways. First, the vortex breakdown bubble changes in size and shape, and is generally wider in the reacting case. Second, the jet spreading angle is higher in the reacting case, presumably because of the wider vortex breakdown bubble. Third, the time-averaged shear layer locations, as shown by the vorticity plots, also spread as a result of the two aforementioned effects. The time-averaged jet velocity is higher in the reacting case, a result of expansion from the flame; the time-averaged shear layer strengths are also greater than in the reacting data. Note that this flow contains two distinct shear layers, one emanating from the inner edge and one from the outer edge of the annulus. The flame configuration is nominally that of a “V-shape” stabilized in the inner shear layer only.

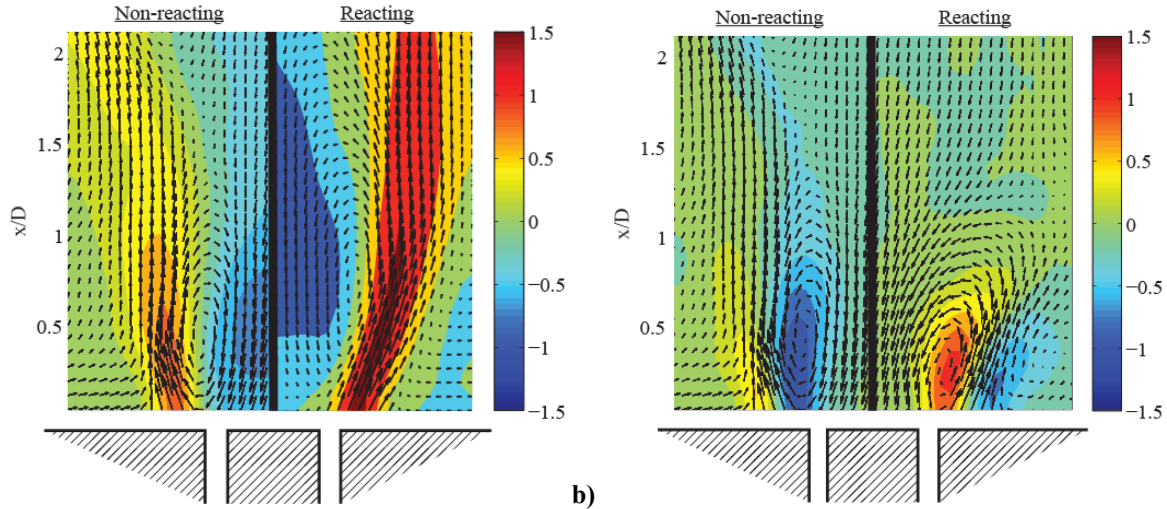
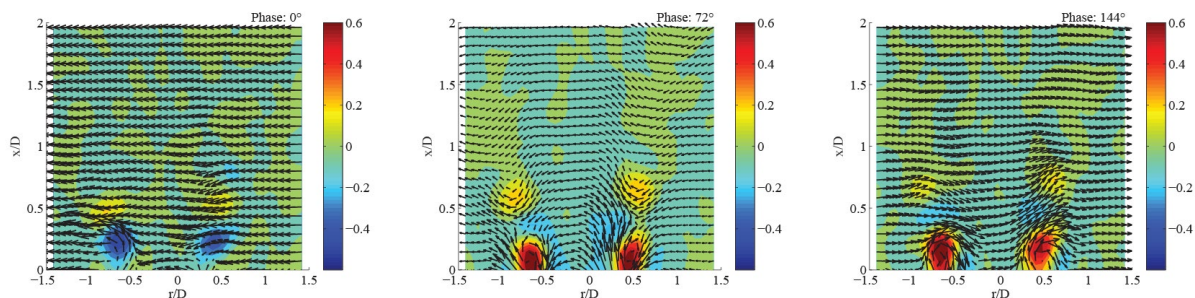


Figure 2. Time-averaged a) axial velocity and b) vorticity fields at $U_o=10$ m/s, swirl number of 0.85, non-reacting flow (left) and reacting flow (right), equivalence ratio of 0.9 with natural gas fuel. Axial velocity is normalized by the bulk velocity, U_o , and vorticity is normalized by the bulk velocity divided by the annular gap width, $U_o/(r_2-r_1)$.

5.2 Effect of amplitude at 400 Hz out-of-phase – non-reacting

In the out-of-phase cases, the nozzle is located at an acoustic velocity anti-node and a pressure node, resulting in an asymmetric velocity disturbance field. This non-axisymmetry in the acoustic field excites a non-axisymmetric response in the shear layers, as is indicated in the phase-averaged vorticity fluctuation plots in Figure 3. These data, taken from the $u_T=4.2$ m/s case for clarity, show a non-axisymmetric pattern in the vorticity fluctuation, as the shear layer sheds in a helix. In a plane of the flow, this vortex rollup looks like alternate vortices shedding from the dump plane on either side of the nozzle centerline. The non-axisymmetry of the flow field is visible in the vorticity contours on either side of the centerline, keeping in mind the 180° offset in vorticity fluctuation magnitude that arises from the differences in sign of vorticity on either side of the centerline. In the flow field far from the nozzle, where the vortical velocity fluctuations have dissipated, the velocity fluctuations predominantly stem from the transverse acoustic field. This is quite evident from the velocity vectors in Figure 3, where the vectors oscillate from pointing almost entirely left (at 0 degrees phase) to entirely right (near 144 degrees phase). Closer to the dump plane, however, the velocity fluctuations are a combination of acoustic and vortical velocity.



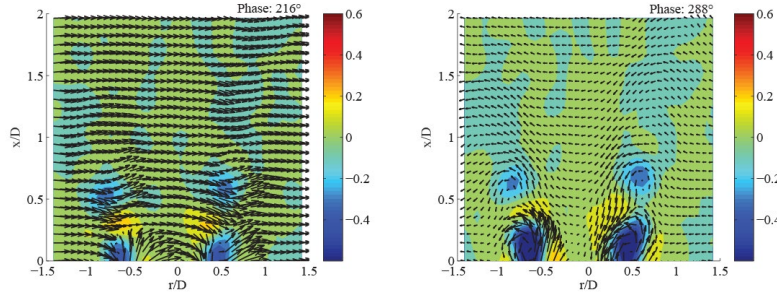


Figure 3. Phase-averaged velocity and vorticity fluctuations at five phases of the acoustic cycle for 400 Hz out-of-phase forcing in non-reacting flow at $U_o=10$ m/s, swirl number of 0.85. Vorticity is normalized by the bulk velocity divided by the annular gap width, $U_o/(r_2-r_1)$.

A POD of this flow field illustrates the effect of amplitude on the flow field, and can, in some cases, separate the contributions of the vortical and acoustic velocity components. Figure 4 shows the percent energy contribution of the first 20 of 500 modes in the POD at four forcing amplitudes. At the lower forcing amplitudes, the energy distributions is relatively flat and the first four modes only contain 11% of the fluctuating energy in the flow. By contrast, the first four modes of the highest forcing amplitude case contain 19% of the fluctuating energy. However, at 42% and 60% transverse forcing amplitude, much of that energy is captured in only the first mode. For the highest amplitude case, the first mode alone contains 11% of the fluctuating energy.

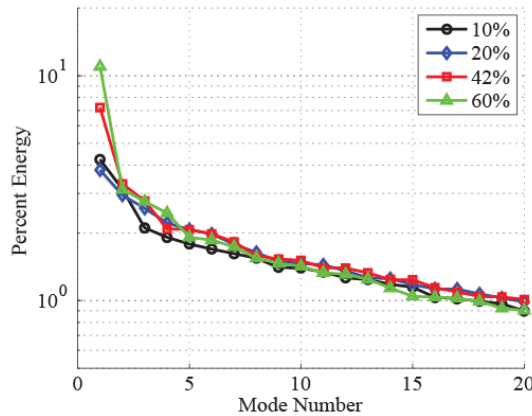


Figure 4. POD energy distribution at 400 Hz out-of-phase forcing for the non-reacting case at $U_o=10$ m/s, swirl number of 0.85.

The spatial modes, shown in Figure 5, highlight the relative contributions of the acoustic and vortical velocity fluctuations. The first four modes (in rows) are shown at four forcing amplitudes (in columns). The first four modes are chosen as the energy contribution of the subsequent modes decreases linearly, as can be seen in Figure 4; the first four modes are representative of both energetic and distinct contributions to the flow oscillations. The 10% forcing amplitude data show little sign of coherent vortical motion in any

one mode, and the temporal modes, discussed below, do not contain much energy at the forcing frequency, 400 Hz. At the 20%, 42%, and 60% forcing amplitudes, vortical motion in the shear layers is evident. This can be seen by the periodic bands of transverse velocity fluctuation that progress downstream of the nozzle, particular in the shear layer region. Previous work has shown that in the presence of acoustic forcing, the shear layer oscillations far outweigh any other vortical oscillation in the flow field; the PVC in this flow field is weak [18]. For the 20% transverse forcing amplitude, vortical motion is found in all four modes. Mode 1 at 20% amplitude also contains a significant number of vectors downstream of the nozzle that oscillate from left to right at the forcing frequency. However, closer to the nozzle, there is clear indication of vortical structures. At the two lower amplitudes, the POD did not separate the acoustic and vortical disturbances into different modes, and as a result, this method would not work for quantifying the relative contribution of these disturbances to the overall disturbance field.

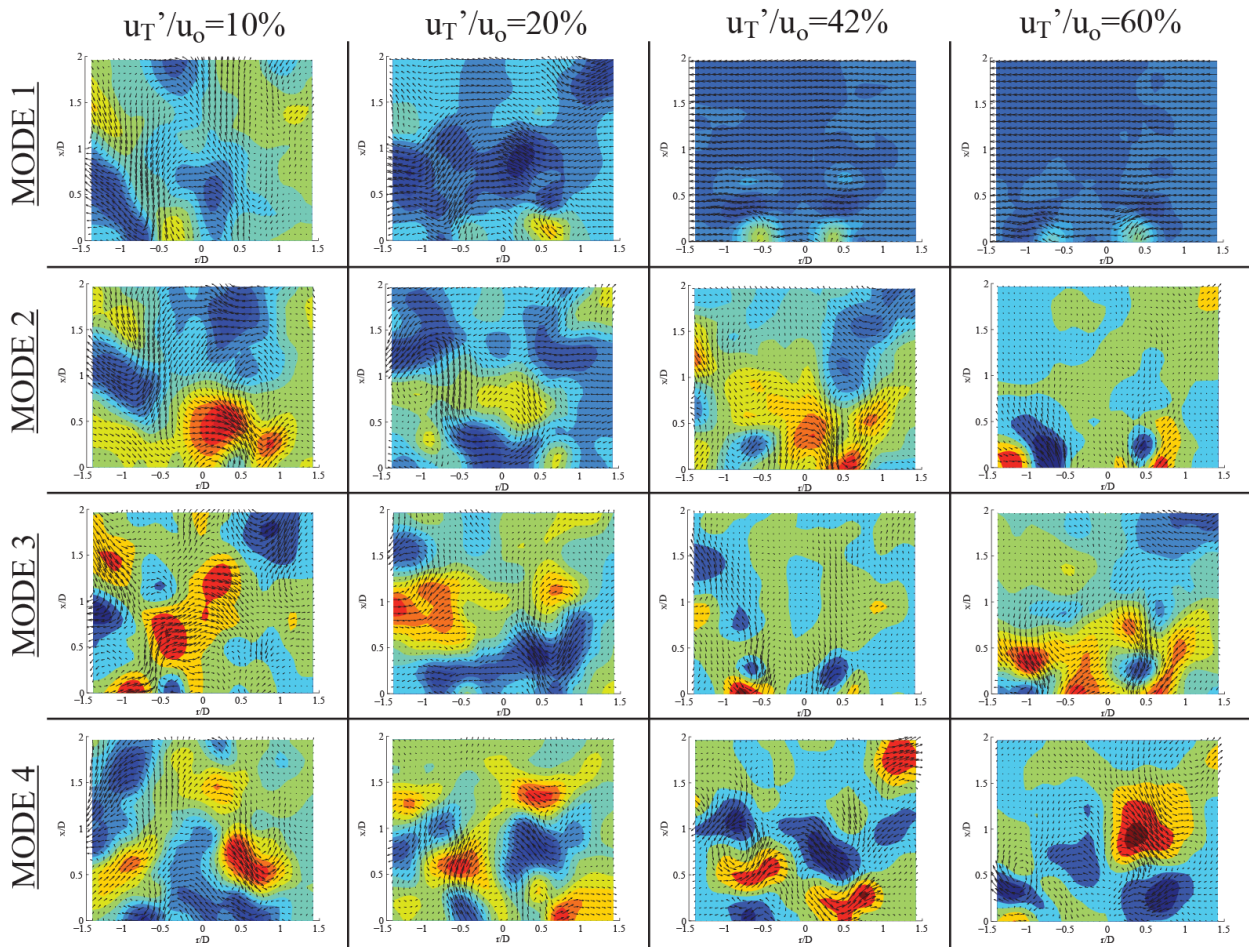


Figure 5. First four spatial POD modes (rows) for 400 Hz out-of-phase forcing at $U_o=10$ m/s, swirl number of 0.85 in non-reacting flow at four forcing amplitudes (columns).

At the two higher amplitudes, however, the POD seems to separate the contributions from the acoustic motions, which are shown in Mode 1, and vortical contributions in the remainder of the modes. In Mode 1 of both cases, the majority of vectors are all pointing in one transverse direction, signaling that these oscillations stem from the transverse acoustic field as no vortical disturbances in the flow field are that uniformly unidirectional. When reconstructed with its temporal mode amplitude, Mode 1 also shows transverse oscillatory behavior in the far field. Closer to the nozzle, the velocity fluctuations in Mode 1 at both 42% and 60% forcing amplitude point in (on the left) and out (on the right) of the nozzle's annular passage. This longitudinal oscillation is an indication of the transverse to longitudinal acoustic coupling at the nozzle exit, or "injector coupling," that has been described in previous work [21]. Vortical velocity fluctuations at the two highest amplitudes are found in Modes 2 and higher, although there may be some acoustic energy in those modes as well. The vortical disturbances are mostly located in the shear layer, which corresponds to the vortical fluctuations that were present in the phase-averaged images in Figure 3.

The spectra of the first four temporal modes at four forcing amplitudes are in Figure 6. Most of the spectra have a peak at 400 Hz, the forcing frequency at this condition. Both acoustic and vortical velocity fluctuations can contribute to this peak because the shear layer instability responds to the acoustics at the forcing frequency. Additionally, some of the modes have some low-frequency content between 0 and 160 Hz. Similar low-frequency content was measured, particularly at low forcing amplitudes, in previous studies of the vortex breakdown bubble in this flow field [18]. These motions are likely due to motion within the vortex breakdown bubble and will not be considered in detail here as they do not play a significant role in the flame response to the transverse acoustic field.

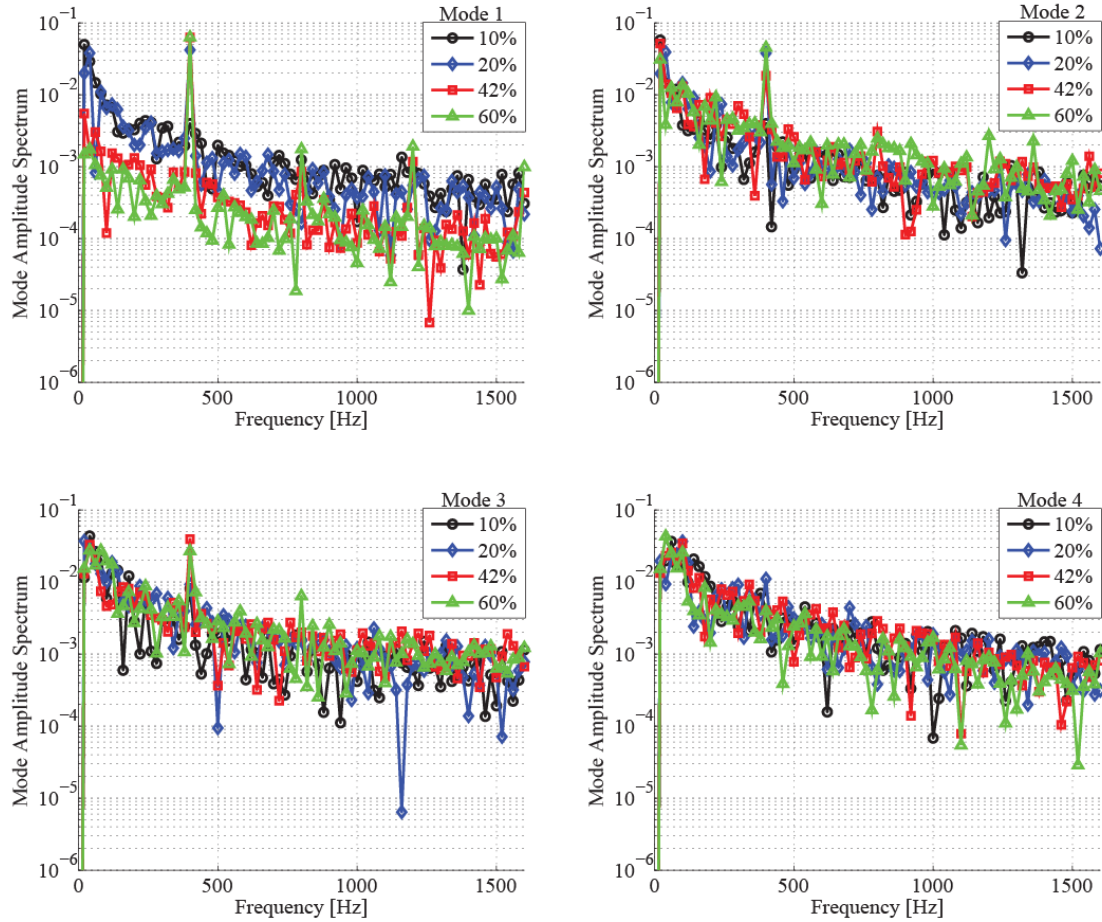


Figure 6. FFTs of the first four temporal POD modes for 400 Hz out-of-phase forcing at $U_o=10$ m/s, swirl number of 0.85 in non-reacting flow.

The Mode 1 spectra show relatively strong 400 Hz oscillations at all four forcing amplitudes, although the oscillations at the 10% forcing amplitude are quite small compared to those of the other three forcing amplitudes. As the forcing amplitude increases, the strength of the 400 Hz peak increases and the low-frequency content is suppressed. This is further evidence that at the two higher forcing amplitudes the velocity fluctuations are predominantly acoustic. The low frequency motion remains in the spectra of the other modes, even at the high forcing amplitudes, but is largely removed from Mode 1. Another feature of the high amplitude spectra is the presence of several harmonics at 800 Hz, 1200 Hz, and 1600 Hz. Analysis of pressure signals has shown that these harmonics most likely stem from non-linearity from the speakers [19].

Focusing now on the Modes 2-4 spectra for the three highest forcing amplitudes, it is evident that the relationship between the 400 Hz signal strength and forcing amplitude is no longer monotonic. For example, the highest 400 Hz peak for Mode 2 is from the 60% amplitude case, followed by the 20% then

the 42% cases in order of reducing strength. The relative strength of the low-frequency content also varies in similar ways for Mode 2. Non-monotonic variation in 400 Hz and low-frequency peak strengths is seen in Mode 3, and in Mode 4, there is very little 400 Hz content and the low-frequency motion dominates. This analysis shows that at high forcing amplitudes, a POD can help to separate the relative contribution of acoustic and vortical velocity fluctuations to the overall fluctuating flow field. The comparisons of the spectra for Mode 1 and Modes 2-4 not only show the relative contribution of the approximate acoustic and vortical components of the velocity fluctuation, but also the frequency content of each signal.

Further evidence of the acoustic versus convective nature of the different modes can be understood by considering the phase roll-off with downstream distance in the shear layers where vortex shedding is occurring at the forcing frequency. The phase roll-off at the forcing frequency can provide two important pieces of information. First, the slope of the phase roll-off with downstream distance can be related to the convective velocity of the disturbances at the forcing frequency, as was done in the two-equation model in Ref. [35]. Second, the relatively phase between the disturbances in the left and right shear layers is indicative of the axisymmetry (or non-axisymmetry) of the disturbances in the shear layers. If the phase difference between the disturbances at a given downstream location is some multiple of 2π , then the shear layers are oscillating out-of-phase, and the disturbance is non-axisymmetric. However, if the phase difference between the disturbances is an odd-multiple of π , then the oscillations are in-phase, and axisymmetric disturbances are present in the shear layers.

For reference, the amplitude and phase of the FFT of the fluctuating velocity, prior to POD, along the jet centerline is shown in Figure 7. This analysis is similar to that in Ref. [35], and is shown here for context. The amplitude of the disturbances at the forcing frequency at all four forcing amplitudes shows a clear interference pattern, as would be expected in a flow field dominated by one standing-wave disturbance and one traveling-wave disturbance. However, it is unclear from these amplitude plots whether the vortical (or convecting) or the acoustic (or standing) disturbance has a higher amplitude. The phase roll-offs in Figure 7b, however, provide this information clearly. The 10% and 20% forcing cases show classic convective phase roll-off. The convective velocities of the disturbances in the region of $x/D=0-0.6$ are 10.2 m/s for the 10% forcing case and 9.2 m/s in the 20% forcing case; these velocities are congruent with the bulk flow velocity, 10 m/s, and the region over which the convective behavior is seen is similar to the regions in Figure 3 where the vortices are still coherent. However, the phase velocity for the two higher amplitude forcing cases, 42% and 60%, is roughly infinite, as is seen by the constant phase as a function of downstream distance. This is indicative of a standing wave, or the transverse acoustic wave, dominating the fluctuations at the forcing frequency.

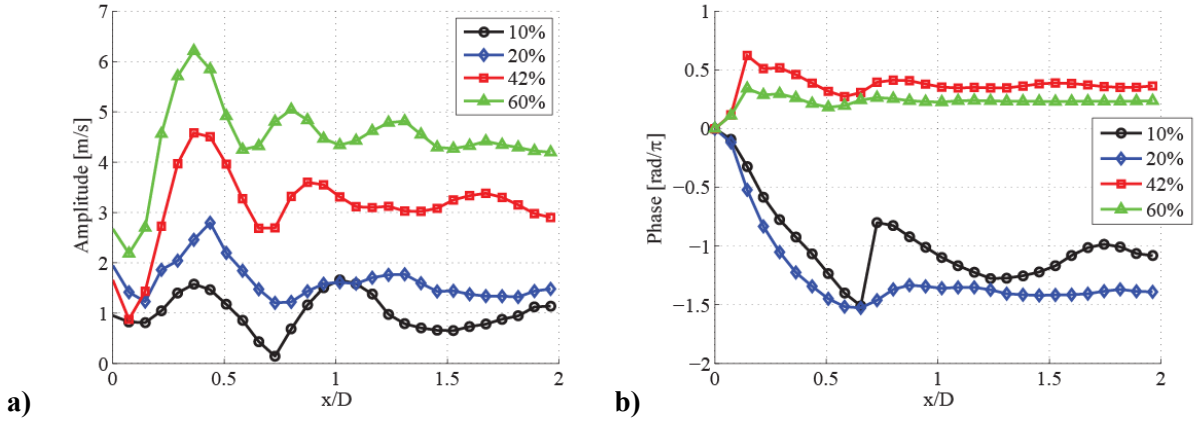


Figure 7. Jet centerline a) amplitude and b) phase roll-off of the transverse velocity fluctuations at the forcing frequency for four transverse forcing conditions.

This same analysis of the phase roll-off of the reconstructed modes shows significant differences between the cases. Figure 8 shows the amplitude and phase of the reconstruction of Mode 1 (a and c, respectively), as well as the amplitude and phase of the reconstruction of the rest of the modes, Mode 2 and higher (b and d, respectively). In this way, we can test if the POD extracted the acoustic oscillations into Mode 1 and left the vortical oscillations, both coherent and turbulent, for the remainder of the modes.

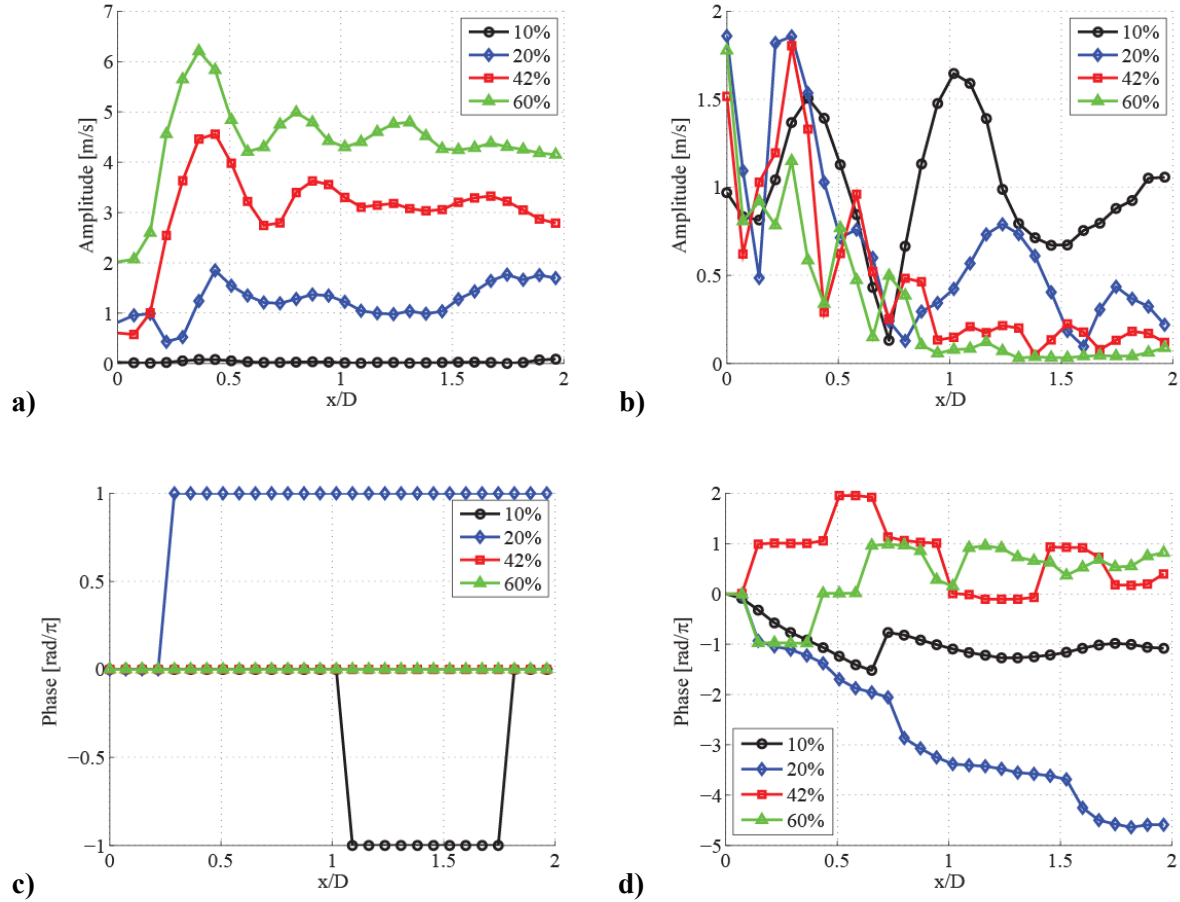


Figure 8. Jet centerline amplitudes and phase roll-offs of the transverse velocity fluctuations at the forcing frequency for four forcing conditions in a) reconstructed Mode 1 and b) reconstruction of the remaining POD modes.

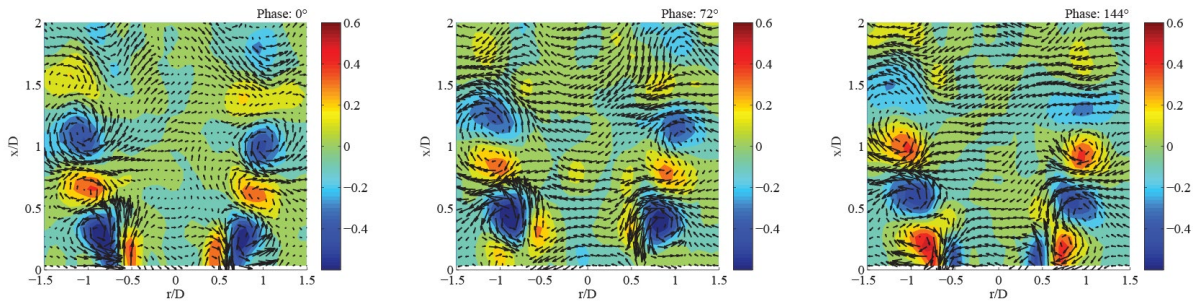
Focusing on the Mode 1 results, both the amplitude and phase curves indicate the relative contribution of acoustic and vortical oscillations at the forcing frequency. First, the amplitude of the 10% forcing case at the forcing frequency is nearly zero; this was also evident in the spectrum in Figure 6a. Since the amplitude of the oscillations is nearly zero, then the phase information is meaningless and should not be considered. On the other hand, the amplitudes of the 42% and 60% forcing cases are comparatively high and follow a similar interference pattern seen in Figure 7. The phase of the oscillations, shown in Figure 8c, is zero for all downstream distances, indicating the presence of an acoustic mode.

The reconstruction of Modes 2-500 shows a very different character than the reconstruction of Mode 1. At the 10% and 20% forcing levels, the amplitude plots show a similar interference pattern to the amplitudes from the non-POD data in Figure 7, and the phase roll-off in Figure 8d is also very similar to the results from the full velocity field. In particular, the phase roll-off between $x/D=0-0.6$ is very similar to that in Figure 7, and the calculated convective velocities of the disturbances at the forcing frequency are 10.1 m/s

and 8.1 m/s for the 10% and 20% cases, respectively. These convective velocities are again congruent with the bulk flow velocity of 10 m/s. The amplitude and phase information of the 42% and 60% forcing cases in Modes 2-500 are significantly less clear than in the Mode 1 reconstruction. The amplitude of the oscillations is much less than that of Mode 1, and the phase jumps between plateaus in steps of approximately π . The phase jumps occur in locations where the fluctuation amplitude rises sharply.

5.3 Effect of amplitude at 400 Hz – reacting

Dynamics of the reacting flow field are temporally similar to those in the non-reacting flow field, as has been discussed in previous studies of this experimental facility [21]. In this configuration, the flame is stabilized in the inner shear layer only and its fluctuations track that of the inner shear layer vortical and acoustic disturbances in the flow field. Figure 9 shows the phase-averaged velocity and vorticity fluctuations for the 400 Hz out-of-phase forcing case in reacting flow. Like the non-reacting case, vortical fluctuations are visible in the shear layers, and transverse motion is visible in the far field, particularly at 144 and 288 degrees phase. The vortical fluctuations are stronger and persist farther downstream in the reacting case than in the non-reacting case, a probable result of the higher mean-shear in the shear layers that was shown in Figure 2. As a result of the stronger vortical fluctuations far from the nozzle, the shape of the transverse acoustic forcing field is not as evident as in the non-reacting case in the phase-averaged images. The non-axisymmetry of the vortex rollup, a result of non-axisymmetric acoustic forcing, is visible in the vorticity contours on either side of the centerline, keeping in mind the 180° offset in vorticity fluctuation magnitude that arises from the differences in sign of vorticity on either side of the centerline.



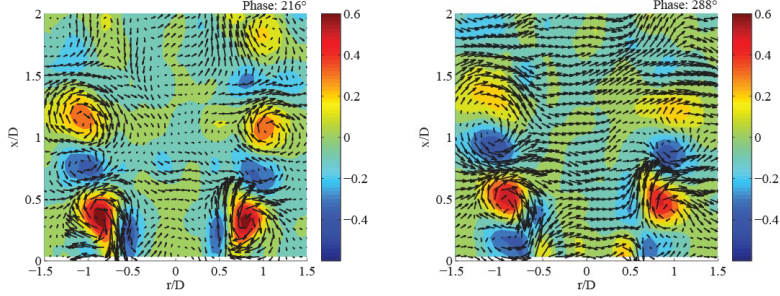


Figure 9. Phase-averaged velocity and vorticity fluctuations at five phases of the acoustic cycle for 400 Hz out-of-phase forcing in reacting flow at $u_r/U_o=42\%$, $U_o=10$ m/s, swirl number of 0.85. Vorticity is normalized by the bulk velocity divided by the annular gap width, $U_o/(r_2-r_1)$.

A POD of the reacting flow field at two forcing amplitudes shows the dominant motions in the flow field. Figure 10 shows a comparison between the energy distribution of the POD in the reacting flow at two forcing amplitudes and the companion non-reacting cases, both at 42% and 60% transverse forcing. The most noticeable difference between the non-reacting and reacting cases is the contribution of Mode 1 at these two high-amplitude forcing conditions. In the non-reacting cases, Mode 1 contributes 7.2% and 11% of the total energy in the 42% and 60% forcing cases, respectively. For the reacting conditions, however, the Mode 1 energies are much lower: 2.1% at 42% forcing amplitude and 3.7% at 60% forcing. The energy distributions for the reacting cases are also flatter than those in the non-reacting cases.

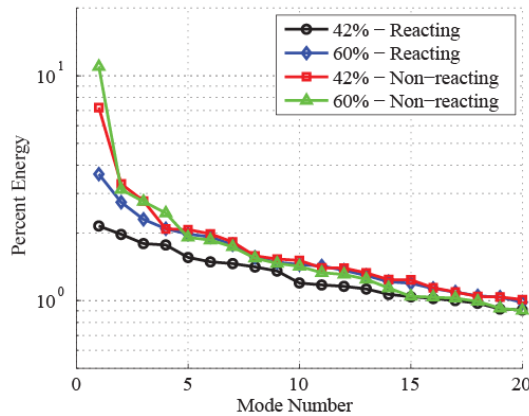


Figure 10. Comparison of the energy distributions for non-reacting and reacting 400 Hz out-of-phase forcing cases at $U_o=10$ m/s, swirl number of 0.85, at two amplitudes.

Figure 11 shows a comparison between the first four non-reacting and reacting spatial modes at two high-amplitude forcing conditions. The non-reacting data are the same as those presented in columns three and four in Figure 5, and here are used in order to determine whether POD can be used to separate the acoustic velocity fluctuations from the vortical velocity fluctuations for a reacting flow case at the same out-of-phase forcing condition. The results in Figure 11 indicate that it is not possible to use the POD to separate these

motions for these reacting cases; in neither the 42% nor the 60% forcing cases does any one mode only contain transverse velocity fluctuations. Each mode in the reacting flow at both forcing amplitudes contains some vortical motion in the shear layers. These vortical fluctuations are similar in form to the phase-averaged results shown in Figure 9, particular at the higher forcing amplitude, and manifest as a train of pockets of transverse velocity fluctuation of opposing sign. Mode 1 for the reacting flow at both 42% and 60% forcing shows significant transverse velocity fluctuation, but vortical fluctuations in the shear layers are superimposed on the acoustic disturbances. The lack of separation between the acoustic and vortical velocity fluctuations is also clear from the temporal mode spectra, shown in Figure 12. Although all five modes at both forcing amplitudes contain a peak at 400 Hz, there is significant low-frequency content in each of the signals, indicative of vortical motion stemming from the recirculation region dynamics.

These differences between the non-reacting and reacting cases at high amplitudes of 400 Hz out-of-phase forcing may be the result of several factors. First, the vortical structures in the shear layer are stronger and survive farther downstream in the reacting case than in the non-reacting case, presumably as a result of the higher level of mean shear. Because these structures have more energy overall, they are likely to have more energy as compared to the transverse acoustic velocity fluctuations at the same forcing amplitude than those in the non-reacting case. This may cause the POD to distribute this high-energy vortical motion into more modes, including in Mode 1. Second, the presence of the flame creates an additional acoustic boundary condition that wasn't present in the non-reacting flow. Acoustic "shielding" [38] and reflections from the sharp temperature gradient of the flame may make the acoustic velocity field more complex and less unidirectional than that in the non-reacting case. There may be other factors that contribute to these differences, and may be the topic of future investigations.

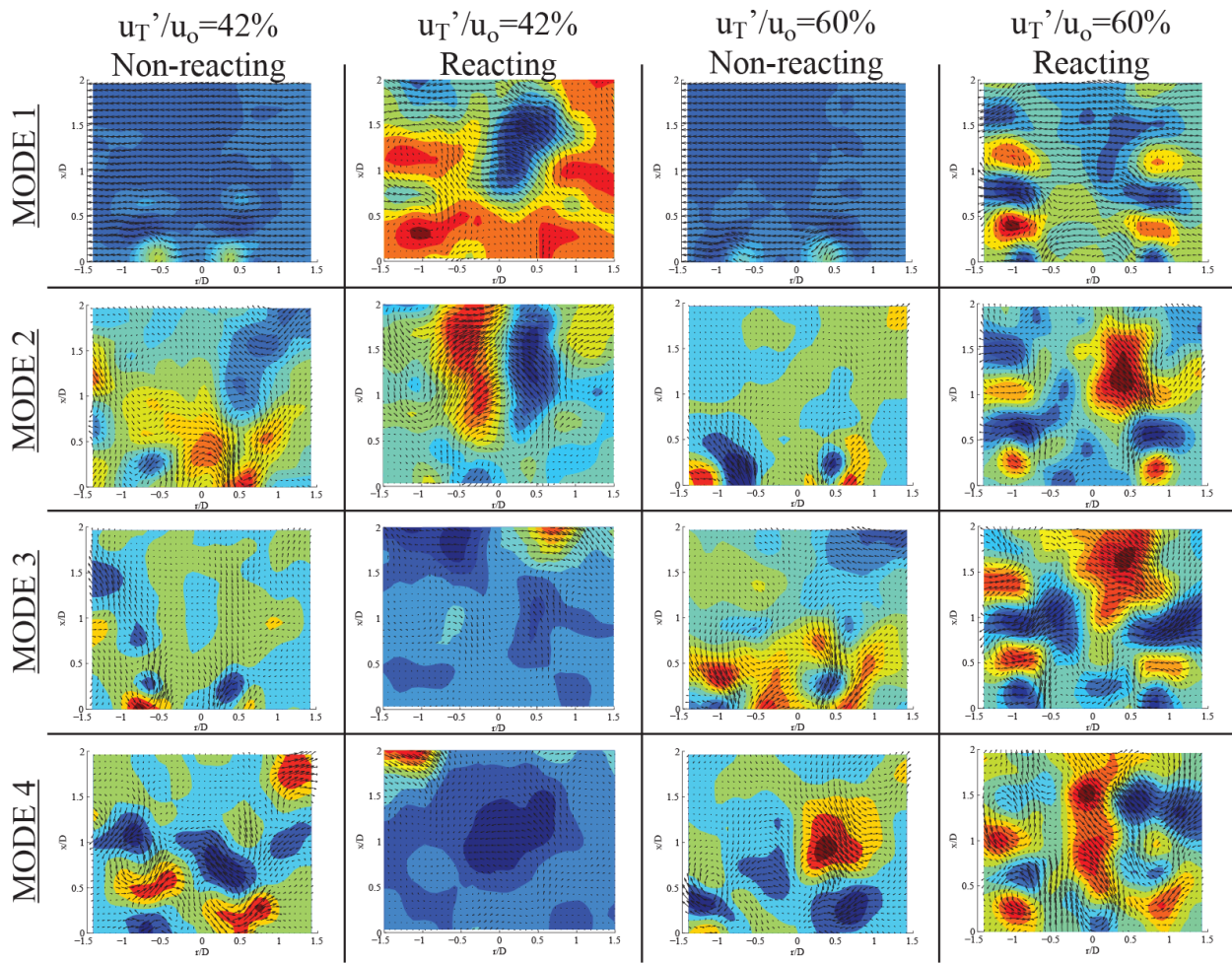
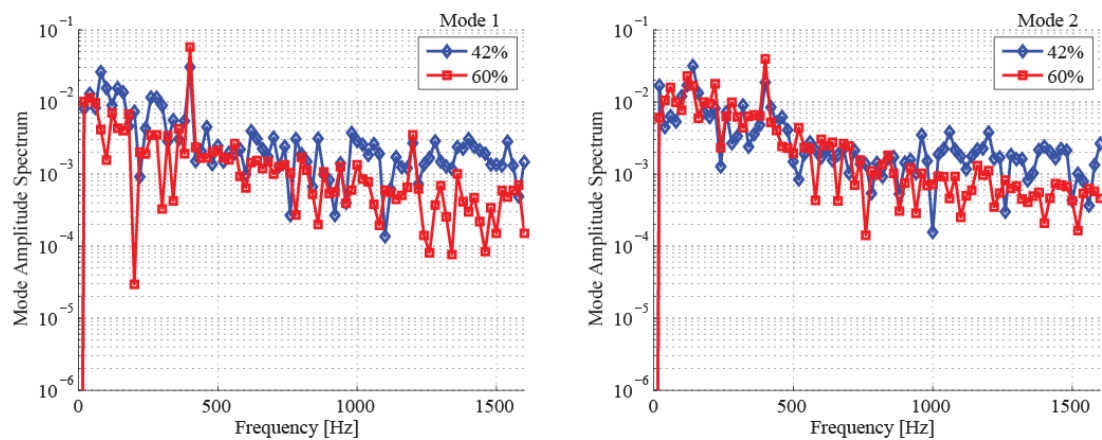


Figure 11. Comparison of the first four spatial modes (rows) for non-reacting and reacting 400 Hz out-of-phase forcing cases (columns) at $U_o=10$ m/s, swirl number of 0.85, at two amplitudes.



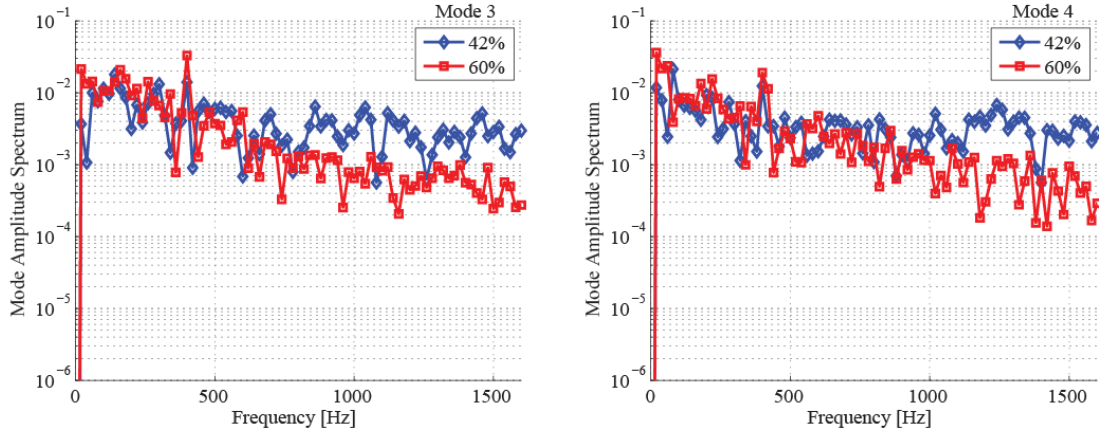


Figure 12. Spectra of the first five temporal modes for reacting 400 Hz out-of-phase forcing cases at $U_o=10$ m/s, swirl number of 0.85, at two amplitudes.

6 Conclusions

This study investigates the effect of transverse acoustic excitation amplitude on both a non-reacting and reacting swirling flow by using proper orthogonal decomposition. In particular, this decomposition is used to understand the relative contributions of vortical and acoustic velocity fluctuations in the flow field that could lead to flame response. Understanding the relative role of these contributions could be an important step towards more accurate reduced-order modeling and validation of higher-order models with this type of high-speed, high-fidelity PIV data. Phase-averaged velocity data across a range of forcing amplitudes show evidence of both vortical and acoustic velocity disturbances in the fluctuating velocity fields. However, extracting the acoustic fluctuations is difficult in the current flow field due to the lack of boundary condition information in the field of view and the disparate length scales between the acoustic and vortical fluctuations.

POD analysis is able to largely separate the acoustic and vortical velocity components for non-reacting, high-amplitude, out-of-phase acoustic forcing cases. The acoustic energy is mostly contained in Mode 1, while the vortical energy is mostly contained in Modes 2-500. This conclusion is supported by the shape of the spatial and temporal parts of Mode 1, as well as the phase roll-off of the reconstructed velocity field from Mode 1. The spatial portion contains almost all vectors pointing in one direction and vectors at the nozzle “breathing” in and out as a result of the transverse to longitudinal coupling. The spectrum of the temporal portion contains a large peak at 400 Hz and almost no other spectral content, whereas the spectra from Modes 2-5 show low-frequency motion resulting from dynamics of the central recirculation zone in addition to a 400 Hz peak. The phase of the fluctuations in Mode 1 is constant as a function of downstream distance, whereas the phase of the reconstructed fluctuations from Modes 2-500 indicate a convective phase

roll-off with convection velocities near that of the bulk flow velocity. Comparison of the vortical and acoustic velocity fluctuations at 400 Hz show that they are comparable in amplitude at these conditions.

POD analysis is not suitable for separating the acoustic and vortical velocity fluctuations in the out-of-phase forcing, reacting flow case. The first four spatial modes showed evidence of vortical motion, although many of them also showed evidence of transverse acoustic motion as well. This may be due to acoustic shielding effects, or to the increased shear strength in the reacting case, resulting in an increased amplitude of the vortical disturbances. If this second explanation is the driving factor, we would expect to see a separation of the acoustic mode at higher forcing amplitudes, as in the non-reacting case. Unfortunately, these amplitudes were not achievable with the current experimental system.

The results of this work show that POD can be used as a tool to help better understand the relative role of acoustic and vortical disturbances in acoustically forced flows, particularly at high amplitudes where the acoustic velocity fluctuations are significant as compared to the vortical velocity fluctuations. However, this work also shows the limitations of this technique, particularly in cases where reactions are present. The failure of the POD as a cut-and-dry decomposition method can be as powerful a result as its success. For example, the appearance of the vortical and acoustic modes simultaneously in the high-amplitude reacting results show that the amplitudes are similar, and that these are highly coupled motions. The eigenvalue decomposition that the POD uses does not discriminate based on any physical processes present in the flow field, and we should not expect it to do so.

Instead, the use of other analytical techniques that are informed by physics may yield better results. For example, the harmonic reconstruction process described in reference to Figure 3 and Figure 9 and a much better way to capture harmonically oscillating phenomena from high-speed velocity data than POD. In this technique, the user is able to choose the frequencies to reconstruct, and so only motions at frequencies of interest are analyzed in the reconstructed data. In this data, the harmonic reconstruction does not adequately aid in the separation of acoustic and vortical motions, as both the acoustic and vortical velocity fluctuations are oscillating at the forcing frequency, and the harmonic reconstruction captures both these modes of motion. As discussed in the introduction, a canonical disturbance decomposition can also be done using the curl and divergence of the fluctuating flow field to separate acoustic and vortical velocity fluctuations. However, this raises two issues in the current data set. First, the wavelengths of the acoustic fluctuations are much longer than the viewing window, meaning that high-frequency noise in the data would easily pollute the long-wavelength acoustic oscillations. The divergence field of data from this experiment has been analyzed at three frequencies, 400, 800 and 1200 Hz, and an acoustic waveform was only recognizable for 1200 Hz in-phase cases where the acoustic wavelength was short and a velocity node was present along

the nozzle centerline. Second, the presence of a flame results in instantaneous dilatation as well, which may pollute the long-wavelength acoustic results from these data.

Going forward, a number of decomposition options can be considered. First, we will continue to strive for methodologies that allow for the use of the curl and divergence fields to be used to decompose the velocity fields for free-shear flows. This methodology follows theory most closely, and provides a most rigorous decomposition. Next, dynamic mode decomposition (DMD) could be used, particularly in cases where the vortical motion is driven by hydrodynamic instabilities [44]. The dynamic mode decomposition provides information about the mode shapes and growth rates, which can be compared to linear stability analysis of the flow field. Some success has been shown in comparing the dynamics of this flow field to hydrodynamic stability analysis [45], and this pathway will also be pursued for future swirling flow studies.

7 Acknowledgements

The data for this work was taken at the Ben T. Zinn Combustion Laboratory at the Georgia Institute of Technology. The author would like to acknowledge Tim Lieuwen, Michael Kolb, and Michael Malanoski for their assistance and discussions in the initial effort for this work.

8 References

1. Ducruix, S., T. Schuller, D. Durox, S. Candel, (2003) "Combustion Dynamics and Instabilities: Elementary Coupling and Driving Mechanisms" *Journal of Propulsion and Power*, **19**(5):722-734
2. Lieuwen, T. and V. Yang, (2005) "Combustion Instabilities in Gas Turbine Engines. Operational Experience, Fundamental Mechanisms and Modeling. Vol. 210" *Progress in Astronautics and Aeronautics* AIAA,
3. Richards, G.A., D.L. Straub, E.H. Robey, (2003) "Passive control of combustion dynamics in stationary gas turbines" *Journal of Propulsion and Power*, **19**(5):795-810
4. Hermann, J. and S. Hoffmann, (2005) "Implementation of Active Control in a Full-Scale Gas-Turbine Combustor" in *Combustion Instabilities in Gas Turbines: Operational Experience, Fundamental Mechanisms, and Modeling*, ed. T. Lieuwen and V. Yang, AIAA, Reston, VA
5. Dowling, A.P. and S.R. Stow, (2003) "Acoustic Analysis of Gas Turbine Combustors" *Journal of Propulsion and Power*, **19**(5):751-764
6. Paschereit, C.O., B. Schuermans, V. Bellucci, P. Flohr, (2005) "Implementation of Instability Prediction in Design: ALSTOM Approaches" in *Combustion Instabilities in Gas Turbine Engines: Operational Experience, Fundamental Mechanisms, and Modeling*, ed. T. Lieuwen and V. Yang, AIAA, Reston, VA
7. Sewell, J. and P. Sobieski, (2005) "Monitoring of Combustion Instabilities: Calpine's Experience" in *Combustion Instabilities in Gas Turbine Engines*, ed. T. Lieuwen and V. Yang, AIAA, Reston, VA
8. Venkataraman, K.K., L.H. Preston, D.W. Simons, B.J. Lee, J.G. Lee, D. Santavicca, (1999) "Mechanism of combustion instability in a lean premixed dump combustor" *Journal of Propulsion and Power*, **15**(6):909-918
9. Hirsch, C., D. Fanaca, P. Reddy, W. Polifke, T. Sattelmayer, (2005) "Influence of the swirler design on the flame transfer function of premixed flames", ASME Turbo Expo, Reno, NV,
10. Palies, P., D. Durox, T. Schuller, S. Candel, (2010) "The combined dynamics of swirler and turbulent premixed swirling flames" *Combustion and Flame*, **157**:1698-1717

11. Thumuluru, S.K. and T. Lieuwen, (2009) "Characterization of acoustically forced swirl flame dynamics" *Proceedings of the Combustion Institute*, **32**(2):2893-2900
12. Ghoniem, A.F., S. Park, A. Wachsmann, A. Annaswamy, D. Wee, H.M. Altay, (2005) "Mechanism of combustion dynamics in a backward-facing step stabilized premixed flame" *Proceedings of the Combustion Institute*, **30**(2):1783-1790
13. Lacarelle, A., T. Faustmann, D. Greenblatt, C.O. Paschereit, O. Lehmann, D.M. Luchtenburg, B.R. Noack, (2009) "Spatiotemporal Characterization of a Conical Swirler Flow Field Under Strong Forcing" *Journal of Engineering for Gas Turbines and Power*, **131**:031504
14. Steinberg, A.M., I. Boxx, M. Stöhr, C.D. Carter, W. Meier, (2010) "Flow-flame interactions causing acoustically coupled heat release fluctuations in a thermo-acoustically unstable gas turbine model combustor" *Combustion and Flame*, **157**(12):2250-2266
15. Cohen, J., G. Hagen, A. Banaszuk, S. Becz, P. Mehta, (2011) "Attenuation Of Combustor Pressure Oscillations Using Symmetry Breaking", 49th AIAA Aerospace Sciences Meeting including the New Horizons Forum and Aerospace Exposition, Orlando, Florida
16. O'Connor, J. and T. Lieuwen, (2012) "Influence of Transverse Acoustic Modal Structure on the Forced Response of a Swirling Nozzle Flow", ASME Turbo Expo, Copenhagen, Denmark
17. Blimbaum, J., M. Zanchetta, T. Akin, V. Acharya, J. O'Connor, D. Noble, T. Lieuwen, (2012) "Transverse to longitudinal acoustic coupling processes in annular combustion chambers" *International journal of spray and combustion dynamics*, **4**(4):275-297
18. O'Connor, J. and T. Lieuwen, (2012) "Recirculation zone dynamics of a transversely excited swirl flow and flame" *Physics of Fluids*, **24**(7):075107-075107-30
19. O'Connor, J. and V. Acharya, (2013) "Development of a Flame Transfer Function Description for Transversely Forced Flames", ASME Turbo Expo, San Antonio, TX
20. Acharya, V., D.-H. Shin, T. Lieuwen, (2012) "Swirl effects on harmonically excited, premixed flame kinematics" *Combustion and Flame*, **159**(3):1139-1150
21. O'Connor, J. and T. Lieuwen, (2011) "Disturbance Field Characteristics of a Transversely Excited Burner" *Combustion Science and Technology*, **183**(5):427-443
22. O'Connor, J. and T. Lieuwen, (2012) "Further Characterization of the Disturbance Field in a Transversely Excited Swirl-Stabilized Flame" *Journal of Engineering for Gas Turbines and Power - Transactions of the ASME*, **134**(1)
23. Hauser, M., M. Lorenz, T. Sattelmayer, (2010) "Influence of Transversal Acoustic Excitation of the Burner Approach Flow on the Flame Structure", ASME Turbo Expo, Glasgow, Scotland,
24. Worth, N.A. and J.R. Dawson, (2013) "Self-excited circumferential instabilities in a model annular gas turbine combustor: Global flame dynamics" *Proceedings of the Combustion Institute*, **34**(2):3127-3134
25. Chu, B.-T. and L.S. Kovásznyai, (1958) "Non-linear interactions in a viscous heat-conducting compressible gas" *Journal of Fluid Mechanics*, **3**(5):494-514
26. Preetham, S. Hemchandra, T. Lieuwen, (2008) "Dynamics of Laminar Flames Forced by Harmonic Velocity Disturbances" *Journal of Propulsion Power*, **24**(6):1390-1402
27. Staffelbach, G., L.Y.M. Gicquel, G. Boudier, T. Poinso, (2009) "Large Eddy Simulation of Self Excited Azimuthal Modes in Annular Combustors" *Proceedings of the Combustion Institute*, **32**:2909-2916
28. Hauser, M., M. Wagner, T. Sattelmayer, (2012) "Transformation of Transverse Acoustic Velocity of the Burner Approach Flow into Flame Dynamics", ASME Turbo Expo, Copenhagen, Denmark
29. Chehroudi, B., D. Talley, J.I. Rodriguez, I.A. Leyva, (2008) "Effects of a Variable-Phase Transverse Acoustic Field on a Coaxial Injector at Subcritical and Near-Critical Conditions", 47th Aerospace Sciences Meeting, Orlando, FL
30. Staffelbach, G., L.Y.M. Gicquel, G. Boudier, T. Poinso, (2009) "Large Eddy Simulation of self excited azimuthal modes in annular combustors" *Proceedings of the Combustion Institute*, **32**(2):2909-2916

31. Ghoniem, A.F., A. Annaswamy, D. Wee, T. Yi, S. Park, (2002) "Shear flow-driven combustion instability: Evidence, simulation, and modeling" *Proceedings of the Combustion Institute*, **29**(1):53-60
32. Koschatzky, V., P. Moore, J. Westerweel, F. Scarano, B. Boersma, (2011) "High speed PIV applied to aerodynamic noise investigation" *Experiments in fluids*, **50**(4):863-876
33. Koschatzky, V., J. Westerweel, B. Boersma, (2011) "A study on the application of two different acoustic analogies to experimental PIV data" *Physics of Fluids (1994-present)*, **23**(6):065112
34. Haigermoser, C., (2009) "Application of an acoustic analogy to PIV data from rectangular cavity flows" *Experiments in fluids*, **47**(1):145-157
35. O'Connor, J. and T. Lieuwen, (2012) "Further characterization of the disturbance field in a transversely excited swirl-stabilized flame" *Journal of Engineering for Gas Turbines and Power*, **134**(1):011501
36. Bechert, D. and E. Pfizenmaier, (1975) "On wavelike perturbations in a free jet travelling faster than the mean flow in the jet" *Journal of Fluid Mechanics*, **72**(02):341-352
37. Berkooz, G., P. Holmes, J.L. Lumley, (1993) "The proper orthogonal decomposition in the analysis of turbulent flows" *Annual Review of Fluid Mechanics*, **25**(1):539-575
38. Ghosh, A., Q. Diao, G. Young, K. Yu, (2006) "Effect of Density Ratio on Shear-Coaxial Injector Flame-Acoustic Interaction", 42nd AIAA/ASME/SAE/ASEE Joint Propulsion Conference & Exhibit, Sacramento, CA
39. O'Connor, J., *Response of a Swirl-Stabilized Flame to Transverse Acoustic Excitation*, Aerospace Engineering Georgia Institute of Technology (2012)
40. Gallaire, F., S. Rott, J.M. Chomaz, (2004) "Experimental study of a free and forced swirling jet" *Physics of Fluids*, **16**:2907
41. O'Connor, J., N.A. Worth, J.R. Dawson, (2013) "Flame and flow dynamics of a self-excited, standing wave circumferential instability in a model annular gas turbine combustor", ASME Turbo Expo, San Antonio, TX,
42. O'Connor, J., V. Acharya, T. Lieuwen, (2015) "Transverse combustion instabilities: Acoustic, fluid mechanic, and flame processes" *Progress in Energy and Combustion Science*, **49**:1-39
43. O'Connor, J. and T. Lieuwen, (2012) "Recirculation zone dynamics of a transversely excited swirl flow and flame" *Physics of Fluids (1994-present)*, **24**(7):075107
44. Schmid, P.J., (2010) "Dynamic mode decomposition of numerical and experimental data" *Journal of Fluid Mechanics*, **656**:5-28
45. Hansford, S., J. O'Connor, K. Manoharan, S. Hemchandra, (2015) "Impact of flow non-axisymmetry on swirling flow dynamics and receptivity to acoustics", ASME Turbo Expo, Montreal, Canada,